Spin Caloritronics in Metallic Superlattices

T. Seki,[1,2,3*] K. Uchida[2,1] and K. Takanashi[4,5]

[1] *Institute for Materials Research, Tohoku University, Sendai 980-8577, Japan*

[2] *National Institute for Materials Science, Tsukuba 305-0047, Japan*

[3] *Center for Science and Innovation in Spintronics (CSIS), Core Research Cluster, Tohoku University, Sendai 980-8577, Japan*

[4] *Advanced Science Research Center, Japan Atomic Energy Agency, Tokai, Ibaraki 319-1195, Japan*

[5] *Advanced Institute for Materials Research, Tohoku University, Sendai, 980-8577, Japan*

*e-mail: takeshi.seki@tohoku.ac.jp

Abstract:

Spin caloritronics, a research field studying on the interconversion between a charge current ($\mathbf{J}_c$) and a heat current ($\mathbf{J}_q$) mediated by a spin current ($\mathbf{J}_s$) and/or magnetization ($\mathbf{M}$), has attracted much attention not only for academic interest but also for practical applications. Newly discovered spin-caloritronic phenomena such as the spin Seebeck effect (SSE) have stimulated the renewed interest in the thermoelectric phenomena of a magnet, which have been known for a long time, *e.g.* the anomalous Nernst effect (ANE). These spin-caloritronic phenomena involving the SSE and the ANE have provided with a new direction for thermoelectric conversion exploiting $\mathbf{J}_s$ and/or $\mathbf{M}$. Importantly, the symmetry of ANE allows the thermoelectric conversion in the transverse configuration between $\mathbf{J}_q$ and $\mathbf{J}_c$. Although the transverse configuration is totally different from the conventional longitudinal

configuration based on the Seebeck effect and has many advantages, we are still facing several issues that need to be solved before developing practical applications. The primal issue is the improvement of conversion efficiency. In the case of ANE-based applications, a material with a large anomalous Nernst coefficient (S_{ANE}) is the key for solving the issue. This review article introduces the increase of S_{ANE} can be achieved by forming superlattice structures, which has been demonstrated for several kinds of materials combinations. The overall picture of studies on spin caloritronics is first surveyed. Then, we mention the pioneering work on the transverse thermoelectric conversion in superlattice structures, which was performed using Fe-based metallic superlattices, and show the recent studies for the Ni-based metallic superlattices and the ordered alloy-based metallic superlattices.

1. Background

1.1 Spin caloritronics

The electron has a spin angular momentum, which is another important character of electron apart from electric charge. Nevertheless, conventional semiconductor technologies have exploited only characteristics of the electric charge, and had ignored the characteristics of electron spin until the discovery of the giant magnetoresistance (GMR) [Refs.1,2]. The discovery of GMR opened up a new research field of electronics, which is called spintronics, and the rapid progress in spintronics led to the new concept of "spin current" [Refs.3.4]. A spin current is the flow of spin angular momentum without accompanying the electric charge flow, and is carried not only by conduction electrons but also by magnons, *i.e.* collective excitation of localized spins. A spin current allows us to develop novel functionalities of spintronic devices, *e.g.* magnetization vector manipulation without external magnetic field [Ref.5] and information transmission in a magnetic insulator [Ref.6]. Thus, a spin current is now regarded as a basis of various spin-related phenomena involving new physics.

As many researchers eagerly studied on how a spin current is created, controlled and detected, the interaction between a spin current and a heat current has also attracted much attention. Spin caloritronics is the research field studying the interconversion between a spin current and a heat current or a charge current and a heat current mediated by magnetization [Refs.7-9]. In 2007, Hatami and coworkers theoretically predicted that the spin-polarized heat current can control the magnetization direction of ferromagnetic body [Ref.10], and this work opened the door of spin caloritronics. Following this theoretical work, the spin Seebeck effect (SSE) was experimentally discovered [Ref.11].

The SSE can be observed in a junction with a magnetic material and a conductor, where a spin current is induced near the junction interface by applying the temperature gradient in the junction. The pioneering study on the SSE was done with the junction consisting of a ferromagnetic metal and a paramagnetic metal [Ref.11]. However, it was demonstrated that the SSE can be observed even in a magnetic insulator [Refs.12,13]. This fact indicates that the SSE is driven by magnons that transmit even in the magnetic insulator. **Fig. 1(a)** is an illustration of the junction with the paramagnetic metal and the magnetic insulator (or the magnetic metal). The temperature gradient (∇T) applied along the perpendicular to the junction interface induces the thermal dynamics of local spins, which results in the magnon-spin current. This magnon-spin current is converted to the conduction electron-spin current ($\mathbf{J}_\mathrm{s}$) at the junction interface via interface exchange interaction, which is characterized as a spin mixing conductance [Ref.14]. Then, this $\mathbf{J}_\mathrm{s}$ is converted to the charge current ($\mathbf{J}_\mathrm{c}$) through the inverse spin Hall effect (ISHE) [Refs.15,16]. ISHE has the symmetry of $\mathbf{j}_\mathrm{c} = (2e/\hbar)\theta_\mathrm{SH}(\mathbf{s} \times \mathbf{j}_\mathrm{s})$, where $\mathbf{j}_\mathrm{c}$ and $\mathbf{j}_\mathrm{s}$ are charge current density and spin current density, respectively, θ_SH is the spin Hall angle, e (< 0) is the electric charge of an electron, $\hbar$ is the reduced Planck constant, and $\mathbf{s}$ represents the quantization axis of spin. In general, the ISHE is observed in various materials with large spin-orbit interaction [Refs.15-21]. The utilization of ISHE allows the electrical detection of the SSE.

The discovery of SSE fascinated many researchers, and spin caloritronics has quickly grown into an interdisciplinary research field. To date, a variety of spin-caloritronic phenomena have been reported: spin-dependent Seebeck effect [Ref.22], spin-dependent Peltier effect [Ref.23], spin Peltier effect [Refs.24,25], and spin Nernst effect [Refs.26,27]. Those newly discovered spin-caloritronic phenomena have stimulated the renewed interest in the thermoelectric phenomena in a magnet that have been known for a long time. The anomalous Nernst effect (ANE) is one of the magneto-thermoelectric effects, details of which will be mentioned in the following subsection.

1.2 Anomalous Nernst effect

The ANE is a thermoelectric effect observed in many magnetic materials [Ref.28]. **Figure 1(b)** displays the symmetry of ANE in a ferromagnetic thin film with spontaneous magnetization (**M**) along the *z* direction (out-of-plane direction of the thin film). When ∇T is applied along the in-plane *x* direction, the charge current flow appears along the in-plane *y* direction. The charge current density driven by the ANE is given by

$$\mathbf{j}_{\mathrm{c}} = \sigma S_{\mathrm{ANE}} \left(\frac{\mathbf{M}}{|\mathbf{M}|} \times \nabla T \right), \tag{1}$$

where S_{ANE} is anomalous Nernst coefficient and σ is electrical conductivity. S_{ANE} is expressed as [Ref.29]

$$S_{\mathrm{ANE}} = \rho_{\mathrm{xx}} \alpha_{\mathrm{xy}} - \rho_{\mathrm{yx}} \alpha_{\mathrm{xx}}, \tag{2}$$

where ρ_{xx}, ρ_{yx}, α_{xx}, and α_{xy} are the longitudinal resistivity, anomalous Hall resistivity, longitudinal thermoelectric conductivity, and transverse thermoelectric conductivity, respectively. The ANE has the reciprocal effect. When the charge current flows, *i.e.* electric voltage difference (ΔV) is applied along the in-plane *x* direction of the ferromagnetic thin film with *z*-directional **M**, the temperature gradient

appears along the in-plane *y* direction. This is called the anomalous Ettingshausen effect (AEE) [Refs.30,31], symmetry of which is given by

$$\mathbf{j}_{\mathrm{q}} = \sigma \Pi_{\mathrm{AEE}} \left(\frac{\mathbf{M}}{|\mathbf{M}|} \times \nabla V \right), \tag{3}$$

where $\mathbf{j}_{\mathrm{q}}$ is heat current density driven by the AEE, Π_{AEE} is the anomalous Ettingshausen coefficient. The coefficients of ANE and AEE have the following relationship: $\Pi_{\mathrm{AEE}} = S_{\mathrm{ANE}} T$ [Ref.31].

An important point is that the ANE allows us to convert heat current into charge current in "transverse configuration" between them, which means that the input direction of heat current is orthogonal to the output direction of charge current [Ref.32]. This configuration is totally different from that of conventional thermoelectric conversion devices based on the Seebeck effect, in which the input of heat current and the output of charge current are aligned in parallel. Thanks to the characteristic transverse configuration of ANE, ANE-based thermoelectric conversion applications have been proposed recently, *e.g.* thermoelectric power generator for tube-shaped heat source [Ref.33], and heat flux sensor [Ref.34].

Considering the above applications, a dimensionless figure of merit (zT) becomes a crucial parameter to determine the performance of the ANE-induced thermoelectric conversion. The zT for the ANE material is expressed as

$$zT = \left(\sigma_{\mathrm{yy}} S_{\mathrm{ANE}}^2 / \kappa_{\mathrm{xx}} \right) \cdot T, \tag{4}$$

where κ_{xx} is the thermal conductivity along the *x* direction and σ_{yy} is the electrical conductivity along the *y* direction. It is noted that the orthogonality between σ and κ frees us from the constraint coming from the Wiedemann–Franz law in anisotropic materials [Ref.35]. In order to improve the value of zT, the primal task is to find materials exhibiting large S_{ANE}. From that point of view, the ANE has been investigated for a variety of materials including ferromagnets, ferrimagnets and antiferromagnets. The

review paper of Ref.28 plotted the reported values of S_{ANE} for various materials. **Table 1** summarized the representative ferromagnetic materials showing S_{ANE} larger than 1 μV K^{-1} at room temperature [Refs.34,36-41]. At present, the largest S_{ANE} has been reported in the Co_2MnGa Heusler alloy [Refs.36,37,42], which is known as a Weyl ferromagnet. Those theoretical and experimental studies suggest that the characteristic electronic structure of Co_2MnGa leads to the large Berry curvature, which is responsible for the enhancement of ANE. Although Co_2MnGa exhibited the large S_{ANE}, its magnitude has not yet reached the level for practical applications. Although several topological materials [Refs.43-46] also exhibit large S_{ANE}, particularly S_{ANE} = 23 μV K^{-1} at 40 K for $UCo_{0.8}Ru_{0.2}Al$ [Ref.45], room temperature operation is desired for practical applications. Thus, it is very crucial to develop a material showing S_{ANE}, at least, one order of magnitude larger than the existing ANE materials, *i.e.* S_{ANE} > 10 μV K^{-1} at room temperature. From **Eq. (4)**, one may see that the increase of σ_{yy}/κ_{xx} is also effective to improve the value of zT, so new materials having a large anisotropy in conductivities between *x* and *y* directions are necessary.

As mentioned above, the increase of S_{ANE} and the increase of σ_{yy}/κ_{xx} are the key points for improving the performance of ANE-induced thermoelectric conversion. The formation of metallic superlattice is regarded as a strategy to this end. The following subsection focuses on what a metallic superlattice is.

1.3 Metallic superlattice

Metallic superlattices, where different kinds of metallic layers are alternated periodically in a nanometer scale, were extensively studied from late 1980's to early 1990's, which led to the discoveries of interface magnetic anisotropy [Ref.46], interlayer exchange coupling [Ref.47], and giant magnetoresistance effect [Refs.1,2]. These phenomena have provided the basis of spintronics. A

research trend has shifted to the spintronics phenomena rather than the materials: metallic superlattices. Even now, however, from the viewpoint of the recent progress of spintronics, we can find the usefulness of metallic superlattices as the materials with assembled interfaces.

At an interface and/or in a reduced dimension, which shows the totally different properties from the bulk properties [Ref.48], we can expect the enhancement of spin-orbit interaction, resulting in the modulation of signal coming from spin-orbit coupling phenomena such as the anomalous Hall effect (AHE) [Ref.49]. Also, we may expect the reduction of thermal conductivity due to the interfacial thermal resistance. Metallic superlattices possess periodic structures. It is natural to consider that such a periodicity modifies the electronic band structure due to the additional boundary condition.

Those characteristics of metallic superlattices may positively influence on the key parameters of S_{ANE} and $\sigma_{\mathrm{yy}}/\kappa_{\mathrm{xx}}$. **Figure 2** depicts the configuration of ANE utilizing the metallic superlattice, in which ferromagnetic layers with **M** and nonmagnetic layers are alternatively stacked. In this configuration, the out-of-plane direction is defined to be the *x* direction, and the temperature gradient is applied along *x*. **M** is pointed along the in-plane *z* direction. Then, the resultant ANE voltage appears along the in-plane *y* direction. Possible advantages for this configuration are as follows. First, the interface-induced spin-orbit interaction may affect the magnitude of S_{ANE}. The periodic layer stacking also modifies the electronic band structure, resulting in the modification of S_{ANE}. If those factors positively contribute to the magnitude of S_{ANE}, a large ANE is expected in the metallic superlattice. Second, the existence of many interfaces gives rise to the large interfacial thermal resistance, which suppresses the thermal conduction and provide the smaller κ_{xx} than the bulk case. In contract to κ_{xx}, the reduction of electrical conductivity along *y*, namely σ_{yy}, is not remarkable because of less interface effect than that along the *x* direction. This corresponds to the anisotropy in conductivities between *x* and *y* that was mentioned in the previous section. Therefore, the formation of metallic superlattice is a

possible strategy to improve the performance of ANE-induced thermoelectric conversion.

In this review article, the pioneering work on the ANE using Fe-based metallic superlattices is first introduced in the next section (**Sec. 2**). Then, the study for the Ni-based metallic superlattices is shown in **Sec. 3**, in which the large α_{xy} comparable to that for the topological materials was observed for the Ni/Pt metallic superlattices. **Section 4** is devoted to the development of ordered alloy-based metallic superlattices. The Co_2MnGa Heusler alloy layers, which is known as a Weyl ferromagnet, were incorporated into the component of metallic superlattice. The combination of ferromagnetic Co_2MnGa and nonmagnetic AlN allows us to obtain large S_{ANE} even for the polycrystalline Co_2MnGa layer thanks to the interface effect. Finally, summary and outlook are given in **Sec. 5**.

2. Pioneering work: Fe-based metallic superlattice

The first experimental work on the ANE for metallic superlattice or multilayered structure was carried out for the Fe-based systems: Fe/Pt, Fe/Au and Fe/Cu [Ref.50]. At that time, the motivation for the work was to examine the contribution of proximity-induced ANE (PANE) [Refs.51,52]. For a paramagnet/ferromagnet junction, in which the paramagnet is near the Stoner ferromagnetic instability, for example Pt and Pd [Refs.53,54], the paramagnet may show ferromagnetism in the vicinity of the paramagnet/ferromagnet interface. This comes from the static magnetic proximity effect. If proximity ferromagnetism and spin-orbit interaction are coupled, the ANE may appear even for paramagnetic materials. A previous study had revealed that proximity-induced magnetic moments in Pt becomes large when Pt is connected to Fe [Ref.55]. Thus, in order to investigate the possible contribution of PANE, we measured the transverse thermoelectric voltage in Fe/Pt metallic superlattices in different magnetization and temperature-gradient configurations by changing the Fe/Pt-interface density. In addition, the same investigation was done for Fe/Au and Fe/Cu metallic superlattices, in which the

proximity-induced magnetic moments in Au and Cu are much smaller than those in Pt.

The Fe/Pt superlattices were grown on the single-crystalline $Gd_3Ga_5O_{12}$ (GGG) (111) substrates employing an ultrahigh vacuum magnetron sputtering system at ambient temperature. This study examined four kinds of Fe/Pt metallic superlattices: Pt (5)/Fe (5), [Pt (2)/Fe (2)]$_{\times 2}$/Pt (2), [Pt (1.25)/Fe (1.25)]$_{\times 4}$, and [Pt (1)/Fe (1)]$_{\times 5}$, where the numbers in parentheses represent the thicknesses in nanometer. Those samples correspond to the superlattices with the numbers of interface N = 1, 4, 7, and 9, respectively. It is noted that the total thicknesses of superlattices are fixed at 10 nm and the total Fe layer thicknesses are almost the same for all the samples, which means that the Fe/Pt-interface density monotonically increases with increasing N. Since the GGG substrate is a paramagnetic insulator, the substrate does not contribute to the ANE signal.

In case of multilayered structures, one should be careful about the superposition of SSE signal on the ANE signal. To discuss the contribution of SSE in Fe/Pt metallic superlattice, we examined two kinds of measurement configurations [Ref.56]: One is an in-plane magnetized (IM) configuration [**Fig. 3(a)**], where **H** was applied parallel to the Fe/Pt interface while∇T was applied perpendicular to the interface. This IM configuration is often used for the longitudinal SSE measurement for a paramagnet/ferromagnet junction [Ref.13]. ∇T leads to $\mathbf{J_s}$ flowing perpendicular to the paramagnet/ferromagnet interface, and the spin polarization of $\mathbf{J_s}$ flowing into the paramagnet is parallel to **M** of the adjacent ferromagnet, which is in-plane magnetized. Considering the symmetry of ISHE (See **Sec. 1.1**), transverse thermoelectric voltage is generated not only from the ANE but also from the longitudinal SSE in the case of IM configuration. The other is a perpendicularly magnetized (PM) configuration [**Fig. 3(b)**]. **H** was applied perpendicular to the Fe/Pt interface while ∇T was applied parallel to the interface. In the PM configuration, the ANE voltage can appear while the longitudinal SSE voltage disappears due to the symmetry of the ISHE. The comparison of the transverse

thermoelectric voltage between the IM and PM configurations allows us to investigate the contribution of ANE and longitudinal SSE separately.

Figures 3(c) and 3(d) show the H dependence of transverse thermopower (S) for the Pt (5)/Fe (5) and [Pt (1)/Fe (1)]$_{\times 5}$ samples measured with the IM and PM configurations, respectively. In this study, S was defined as $S = (V/\Delta T)(L_z/L_y)$ for the IM configuration and $S = (V/\Delta T)(L_x/L_y)$ for the PM configuration, where ΔT is the temperature difference and the lengths of the GGG substrates along the x, y, and z directions (L_x, L_y and L_z) are L_x = 2 mm, L_y = 6 mm, and L_z = 1 mm. The in-plane magnetization curves are also displayed for comparison. Both Pt (5)/Fe (5) and [Pt (1)/Fe (1)]$_{\times 5}$ samples show clear S signals, in which the sign changes occur in response to the magnetization reversal observed in the magnetization curves. One can see that the magnitude of S increases for both IM and PM cases with increasing the number of N from 1to 9. S_0 is the anomalous component of S, which does not include the ordinary Nernst contribution and is obtained by extrapolating the values of S above saturation magnetic field to zero H.

Figures 4(a) and 4(b) plot the values of S_0 as a function of N in the IM and PM configurations, respectively, in which the results for several different systems are compared: Fe/Pt, Fe/Au, and Fe/Cu metallic superlattices. First, let us focus on the results of Fe/Pt metallic superlattices. S_0 increases roughly in proportion to N in both IM and PM configurations. When the value of S_0 was normalized by the sheet resistance (R_S), which represents the charge current generated by the ANE per unit temperature difference, S_0 / R_S also increases with N [see **Figs. 4(c) and 4(d)**] These experimental facts suggest the strong correlation between the ANE and the Fe/Pt-interface density. Next, the results of Fe/Pt metallic superlattices are compared with the other systems. One can see that even for the Fe/Au, and Fe/Cu metallic superlattices, clear S_0 signals appear and the values of S_0 increase with N as in the case of Fe/Pt. It is noted that S_0 / R_S is more essential than S_0 to compare the ANEs in these metallic superlattices since

S_0 / R_S takes into account the correction coming from the difference in the electrical conductivity between Pt, Au, and Cu and the resultant short-circuit effects approximately as discussed in the original article [Ref.50]. Since the magnitudes of S_0 / R_S for all the samples were comparable at each N value in the PM configuration, we concluded that the main contribution to the ANE enhancement is not the magnetic proximity effect.

One may be aware that the values of S_0 obtained by the IM configuration are smaller than those for the PM configuration. In the case of IM configuration, the temperature gradient in the multilayer is smaller than that in the total system of the multilayer and substrate because of the difference in their thermal conductivities. In contrast to the IM configuration, the PM configuration shows that the temperature difference between the ends of the multilayer film is the same as that of the substrate, since both the film and substrate are directly connected to the heat baths. In the PM configuration, therefore, the actual ∇T in the multilayer is comparable to the ∇T applied to the system. This problem does not allow us to compare the magnitude of S_0 between the IM and PM configurations.

The experimental facts clearly indicate that the ANE is enhanced in alternately stacked paramagnet/ferromagnet systems even in the absence of proximity ferromagnetism. This pioneering work discussed the following four possible explanations for the enhanced ANE in the metallic superlattices: (i) a surface-roughness-induced spin-orbit interaction in the Fe layers, (ii) interdiffusion and alloying at the paramagnet / Fe interfaces, (iii) strain in the Fe layers, and (iv) crystal-symmetry breaking at the paramagnet / Fe interfaces. Considering the universal enhancement of ANE regardless of the kind of nonmagnetic material, at least explanation (i) contributes to the enhancement of ANE.

After the report on the ANE for the Fe-based metallic superlattices, C. Fang and coworkers reported the systematic study on the ANE, the AHE, and the Seebeck effect for the Co/Pt metallic superlattices [Ref.57]. The authors prepared [Co (t_{Co})/Pt (t_{Pt})]$_{\times n}$ on a Si(500 μm)/SiO_2(500 nm) substrate,

where $t_{Co} = t_{Pt}$, $n = 1 – 8$ and $t_{Co} = 12/n$. They found that the anomalous Nernst coefficient increased by 350% as n was increased from 1 to 15, and mentioned that the interfacial contact with Pt was effective to enhance the ANE for the Co-based superlattice systems.

Apart from the superlattice structures with 3d transition metals, there are several reports on the transverse thermoelectric conversion in the multilayers with ferromagnetic oxide layers. R. Ramos and coworkers found the unconventional scaling and significant enhancement of the SSE in Fe_3O_4/Pt multilayers [Refs.58,59]. The reciprocal phenomenon of SSE, that is the spin Peltier effect, was also enhanced in the Fe_3O_4/Pt multilayers [Ref.60]. In addition, the interface-induced ANE was reported for the Fe_3O_4/Pt-based heterostructures [Ref.61].

The early works introduced in this section successfully demonstrated that the formation of metallic superlattice is an effective way to increase the ANE for the several systems. In addition to the increase in the ANE, one may anticipate the suppression of thermal conduction in the perpendicular direction to the layer stacking as mentioned in **Sec. 1**. Very recently, by employing the IM configuration and the time-domain thermoreflectance (TDTR) method, transverse thermoelectric coefficient, in-plane electrical conductivity (σ_{yy}), and out-of-plane thermal conductivity (κ_{xx}) were evaluated for the Fe/Pt metallic superlattices, and the suppression of κ_{xx} due to the formation of superlattice was successfully observed [Ref. 62]. The study of Ref. 62 used the Fe/Pt metallic superlattices with the total thickness of approximately 200 nm, which was much larger than the 10 nm-thick samples shown in this section. As in the case of 10 nm-thick samples, the 200 nm-thick samples showed the monotonic increase in the transverse thermoelectric coefficient with the interface density. This fact indicates that the interface density is a major parameter to increase the transverse thermoelectric coefficient even for the thick metallic superlattices.

3. Ni-based metallic superlattice

The early works shown in **Sec. 2** revealed the enhancement of ANE, particularly for the Fe-based systems. **Sec. 3** focuses on Ni as a ferromagnetic layer of metallic superlattice. Ni exhibits the large anisotropic magneto-Peltier effect thanks to its characteristic electronic structure [Refs.63,64]. Also, that is an interesting material from the viewpoint of the ANE. As a nonmagnetic material, Pt was selected because the large ANE enhancement was reported in the Fe-based and Co-based metallic superlattices as introduced in **Sec. 2**, which is attributable to the large spin-orbit interaction. Then, the ANE was investigated in the Ni/Pt (001) epitaxial superlattices with various Ni layer thicknesses (t_{Ni}) in Ref. 65.

[Ni(t_{Ni})/Pt(1.0 nm)]$_{\times n}$ metallic superlattices were epitaxially grown on $SrTiO_3$ (100) single crystal substrates employing magnetron sputtering. The Ni layer was first deposited at 400ºC, which was followed by the layers of [Pt/Ni]$_{\times n-1}$/Pt deposited also at 400ºC. Finally, a 2-nm-thick Al layer was deposited at room temperature as a capping layer. The deposition temperature of 400 °C was necessary to achieve the (001) epitaxial growth, and the well-defined layered structures were achieved without remarkable intermixing between the layers [Ref.66]. t_{Ni} was set to be 1.5, 2.0, 3.0, and 4.0 nm, where n was set to be 8, 7, 5, and 4, respectively. Those repetition numbers were adjusted for the total thicknesses of approximately 20 nm. All the films exhibited that the easy magnetization axes were the out-of-plane direction, *i.e.* perpendicularly magnetized Ni/Pt metallic superlattices.

For measuring the ANE of Ni/Pt metallic superlattices, the PM configuration was employed. As explained in **Sec. 2**, the ANE voltage can appear while the longitudinal SSE voltage disappears in the PM configuration. Then, the PM configuration allows us to evaluate the transverse thermoelectric signal coming from only the ANE in the Ni/Pt metallic superlattices. **Figure 5 (a)** displays the measurement setup with the PM configuration, and **Fig. 5 (b)** shows the transverse electric field detected

in the in-plane *y* direction, which comes from the ANE (E_{ANE}), divided by the in-plane *x*-directional ∇T as a function of out-of-plane (z-directional) H for the sample with t_{Ni} = 3.0 nm. The square-shaped hysteresis of $E_{\mathrm{ANE}}/\nabla T$, which originates from the magnetization reversal process, was observed. In order to estimate S_{ANE}, E_{ANE} as a function of ∇T was investigated. The slope of E_{ANE} versus ∇T corresponds to S_{ANE}. **Figure 5 (c)** plots the t_{Ni} dependence of S_{ANE}. All the samples exhibit the large values of $S_{\mathrm{ANE}} \geq$ 0.9 μV K^{-1}, and the maximum value of S_{ANE} was obtained to be 1.14 ± 0.05 μV K^{-1} for t_{Ni} = 2.0 nm. It is noted that these values of S_{ANE} for the Ni/Pt metallic superlattices are one order of magnitude of larger than that for the bulk Ni [Refs.38,67].

As shown in Eq. (2), S_{ANE} is composed of two terms: $\rho_{\mathrm{xx}}\alpha_{\mathrm{xy}}$ and $\rho_{\mathrm{yx}}\alpha_{\mathrm{xx}}$. Here, $\rho_{\mathrm{yx}} = -\rho_{\mathrm{xy}} = \sigma_{\mathrm{xy}}/\sigma_{\mathrm{xx}}^2$, where σ_{xx} and σ_{xy} are the longitudinal conductivity and the transverse conductivity, respectively. The term of $\rho_{\mathrm{yx}}\alpha_{\mathrm{xx}}$ comes from the Seebeck effect-induced longitudinal charge current and the resultant transverse voltage through the AHE, *i.e.* $-S_{\mathrm{SE}}\rho_{\mathrm{yx}}/\rho_{\mathrm{xx}} = S_{\mathrm{SE}}\rho_{\mathrm{xy}}/\rho_{\mathrm{xx}}$, where S_{SE} represents the Seebeck coefficient and $\rho_{\mathrm{xy}}/\rho_{\mathrm{xx}}$ corresponds to the anomalous Hall angle. The term of $\rho_{\mathrm{xx}}\alpha_{\mathrm{xy}}$ expresses the direct generation of transverse charge current originating from transverse thermoelectric conductivity. **Figures 5(d), 5(e), 5(f), 5(g) and 5(h)** show the t_{Ni} dependence of S_{SE}, $\rho_{\mathrm{xy}}/\rho_{\mathrm{xx}}$, $\rho_{\mathrm{xy}}\alpha_{\mathrm{xx}}$, α_{xy} and ρ_{xx}, respectively. From **Fig 5. (f)**, it was found that $\rho_{\mathrm{xy}}\alpha_{\mathrm{xx}}$ is two orders of magnitude smaller than S_{ANE}. This indicates that the conversion process through the Seebeck effect followed by the AHE hardly contributes to the ANE of the Ni/Pt metallic superlattices. Since the anomalous Hall angle of Ni/Pt metallic superlattices is not so small compared to other ferromagnets, the small S_{SE} is the reason for the small values of $\rho_{\mathrm{xy}}\alpha_{\mathrm{xx}}$. As shown in **Fig. 5(g)**, the values of α_{xy} have been estimated using the parameters of S_{ANE}, ρ_{xx}, ρ_{xy}, and S_{SE}, which were experimentally obtained and given in **Fig. 5**. One can see the large α_{xy} for the Ni/Pt superlattices. The maximum value was obtained to be α_{xy} = 4.8 A K^{-1}m^{-1} at t_{Ni} = 4.0 nm, which is comparable to or larger than that for the

large ANE materials such as Co_2MnGa (2.4–3.0 A $K^{-1}m^{-1}$) [Ref.36], $Co_3Sn_2S_2$ (~2 A $K^{-1}m^{-1}$) [Ref.43] and $SmCo_5$ (4.6 A $K^{-1}m^{-1}$) [Ref.38].

In **Sec. 2**, the Fe/Pt, Fe/Au, and Fe/Cu metallic superlattices showed the increase in transverse thermopower with increasing the numbers of interfaces, *i.e.* with decreasing the layer thicknesses. In contrast to the case of Fe-based system, S_{ANE} for the Ni/Pt metallic superlattices does not increase remarkably as t_{Ni} is decreased. This experimental result is not explained by the interface contribution. In order to consider another possible contribution, the first-principles calculations were done for σ_{xy} and α_{xy}. α_{xy} is expressed as [Ref.68]

$$\alpha_{\mathrm{xy}} = -\frac{\pi^2}{3}\frac{{k_{\mathrm{B}}}^2 T}{e}\left(\frac{\partial \sigma_{\mathrm{xy}}}{\partial \varepsilon}\right)_{E_{\mathrm{F}}}, \qquad (4)$$

where k_{B} is the Boltzmann constant and $\left(\partial\sigma_{\mathrm{xy}}/\partial\varepsilon\right)_{E_{\mathrm{F}}}$ is the energy derivative of σ_{xy} at the Fermi level (E_{F}). For the details of calculation methods and calculation results, see the original paper [Ref.65]. The fine oscillatory behavior was observed in σ_{xy} as a function of chemical potential (μ) when the superlattice structures were formed. Because this feature was not observed in the case of bulk Ni, the oscillation is attributable to the formation of interfaces. This oscillation in σ_{xy} against μ leads to the increase in energy derivative of σ_{xy}. The band-folding effect provides many band dispersions around E_{F} in the (k_{x}, k_{y}) plane (corresponding to in-plane wave vectors) and the hybridizations of these bands lead to many band splittings. This is the origin for the oscillation in the Berry curvature, and the resultant oscillatory behavior in σ_{xy}. These results suggest that the oscillatory behavior in σ_{xy} due to the interface formation is related with the enhancement of ANE in the Ni/Pt metallic superlattices. For quantitative comparison and more concrete examination, further systematic studies including the effects of structural imperfections and/or phonon/magnon excitations are required.

This section was devoted to the ANE in the Ni/Pt metallic superlattices. Although the

enhancement of ANE was observed by forming the superlattice structure even for the Ni-based system, the tendency in S_{ANE} versus the layer thicknesses for the Ni/Pt was different from the case of Fe-based systems. The enhanced ANE comes from the large α_{xy} in the case of Ni/Pt metallic superlattices.

4. Co_2MnGa-based metallic superlattice

For the research topics given in **Secs. 2 and 3**, 3d transition elements of Fe and Ni were used as ferromagnetic layer materials in metallic superlattices. Although the values of S_{ANE} were successfully enhanced owing to the formation of metallic superlattices, those are too low to apply them to practical devices. In order to realize further increase in S_{ANE} for a superlattice structure, **Sec. 4** introduces the study on metallic superlattices with a topological material.

Co_2MnGa (CMG) Heusler alloy is a ferromagnet with symmetry-protected topological states in the electronic band structure [Refs.36,37]. Thanks to the characteristic electronic band structure, CMG exhibits the large ANE [Refs.36,37,42,69,70] as well as the large AHE [Refs.36,37,69,71] at room temperature. The high atomic ordering such as the B2 or $L2_1$ ordered structure is essential for the formation of electronic states with nontrivial topology [Refs.37,71,72]. Thus, large ANE of CMG has been demonstrated either for single crystalline bulks or for epitaxial films deposited at elevated temperatures on single-crystalline substrates [Refs.36,37,42,69,70].

Although CMG is a candidate as a ferromagnetic layer incorporated into a metallic superlattice structure, it is challenging to find an appropriate nonmagnetic spacer layer for multilayering with CMG layers. Spacer layer materials should satisfy the following requirements: high thermal stability and limited interdiffusion at the interface with CMG. Aluminum nitride (AlN) is one of the III–V compound semiconductors with a wurtzite crystalline structure [Refs.73-75]. Since AlN exhibits excellent mechanical shock resistance, high thermal stability, low expansion coefficient, and low

temperature preparation on flexible substrates, AlN layers have been widely utilized for wearable device applications. For several kinds of multilayer systems, moreover, atomically sharp and smooth interfaces with good uniformity were reported even after a high temperature annealing process [Refs.76,77]. These features make AlN a candidate nonmagnetic spacer layer material for combining with the CMG layer in the multilayered form.

Hereafter, the study on ANE for the CMG/AlN multilayers [Ref.78] is introduced. Because AlN shows the insulative characteristics, strictly speaking, the combination of CMG and AlN is not the metallic superlattice. In this review article, however, multilayered structures with a "metallic" ferromagnetic layer are involved as metallic superlattices.

The multilayer films consist of AlN (20.0 nm)/ [CMG (t_{CMG})/AlN (5.0 nm)]$_{\times n}$ with t_{CMG} = 2.5, 5.0, 12.5, and 25.0 nm, which were fabricated on thermally oxidized silicon substrates at room temperature. The repetition number of multilayering (n) was set to be 25/t_{CMG}. The AlN layers were grown by dc reactive magnetron sputtering from an Al target in an Ar/N2 (3:1) mixture atmosphere and the working pressure was about 0.18 Pa. On the other hand, the CMG layers were fabricated by dc magnetron sputtering from a $Co_{42}Mn_{25}Ga_{33}$ alloy target. The composition for the deposited CMG was determined to be $Co_{52}Mn_{22}Ga_{26}$. All the samples were subsequently post-annealed at 500 ºC in a vacuum furnace for 3 h in order to promote the atomic ordering [Refs.71,79].

Figure 6(a) displays the cross-sectional high-resolution transmission electron microscopy (HR-TEM) image for the sample with t_{CMG} = 12.5 nm. There is no remarkable interdiffusion between the CMG and the AlN layers, namely the sharp interfaces are formed even after the post-annealing at 500 ºC. Compared to the result for the sample with t_{CMG} = 25.0 nm, as shown in **Figs. 6(b) and 6(c)**, the fast Fourier transform (FFT) images for the CMG and AlN layers indicate that the AlN layer deposited on the CMG layer improved the c-axis texture. This means that the highly oriented AlN layers serve as

a texture template for the CMG layers. In addition to the improved (110) texture for CMG layers, the 200 superlattice diffractions suggesting the B2-ordering of CMG are clearly observed for the sample with t_{CMG} = 12.5 nm. With the calculated lattice spacings from HR-TEM and graphic orientation identified from FFT images, the highly oriented CMG/AlN stack involves the structure with the following epitaxial relationship at the interface: $(110)_{CMG} \parallel (0001)_{AlN}$, $[001]_{CMG} \parallel [10\text{-}10]_{AlN}$. The detailed analysis of strain distribution in the CMG layer revealed that a uniform and positive in-plane strain is induced.

All the samples clearly exhibited the transverse electric field due to the ANE. **Figure 6(d)** plots S_{ANE} as a function of t_{CMG}. A relatively high S_{ANE} = 3.8 μV K^{-1} was obtained for the sample with t_{CMG} = 25.0 nm. This S_{ANE} value is close to the reported values for $L2_1$-ordered single crystalline CMG bulks and epitaxial films (see the values for single crystalline and epitaxial CMS given in **Table 1**), suggesting that the sandwiched structure with AlN is effective to increase S_{ANE}. A remarkable point in **Fig. 6(d)** is that the samples with t_{CMG} = 5.0 nm and 12.5 nm show larger S_{ANE} (4.9 μV K^{-1}) than that for t_{CMG} = 25.0 nm. As in the case of Ni/Pt metallic superlattices given in **Sec. 3**, the values of S_{ANE} were decomposed into two terms, $\rho_{xx}\alpha_{xy}$ and $\rho_{xy}\alpha_{xx}$, using Eq. (2) in order to understand the characteristic thickness dependence. The detailed analysis enables us to find that S_{SE} is increased at t_{CMG} = 5.0 nm and 12.5 nm, which plays the primary role for the enhanced S_{ANE} for t_{CMG} = 5.0 nm and 12.5 nm. As discussed above, the uniform and positive in-plane strain exists inside the CMG layers with the appropriate thicknesses such as t_{CMG} = 12.5 nm. Previous works [Refs.80-82] highlighted the influence of strain on the electronic structure, giving rise to the modulation of thermoelectric properties including the Seebeck coefficient. Thus, this work suggests that the remarkable tensile strain coming from the epitaxial growth is a possible scenario to explain the increase in S_{SE}.

This section introduced that the large S_{ANE} was achieved even for the polycrystalline CMG

layer grown on the non-single-crystal substrate by multilayering with the AlN nonmagnetic layer. Since this growth technique does not require the single crystal substrate, the CMG/AlN stack can be prepared not only on rigid substrates but also on a flexible substrate [Ref.78]. Even on a flexible polyimide (PI), the CMG/AlN stack showed S_{ANE} = 4.7 ± 1.0 μV K^{-1}. This experimental fact suggests that the combination of CMG and AlN is a potential materials combination for flexible spin-caloritronic devices. At present, we have no definite idea if this multilayering is applicable to other Heusler alloys. Because there are several Heusler alloys exhibit the large ANE such as $Co_2Mn(Al,Si)$ [Ref.29], other combinations will be interesting research targets to examine the effect of multilayering.

5. Summary and Outlook

This article reviewed the recent progress in the spin caloritronic study, particularly by focusing on the topics of the ANE using the metallic superlattices: Fe-based [Ref.50], Ni-based [Ref.65], and ordered alloy-based [Ref.78] metallic superlattices. The study on Fe-based metallic superlattices such as Fe/Pt, Fe/Au, and Fe/Cu indicated the significant impact of interface on the magnitude of ANE, and proposed a possible scenario of surface-roughness-induced spin-orbit interaction in the Fe layers as an explanation for the enhancement of ANE regardless of the kind of nonmagnetic material. In the case of Ni-based metallic superlattices, that was Ni/Pt, the enhanced ANE came from the large α_{xy}. The experiment and theoretical calculation suggested that the oscillatory behavior in σ_{xy} due to the interface formation leads to the increase in α_{xy}, resulting in the enhancement of ANE. By multilayering CMG and AlN, the large ANE was achieved even for the polycrystalline CMG layers thanks to the formation of highly ordered structure and the increased Seebeck effect, which is attributable to the remarkable tensile strain coming from the interface due to the epitaxial growth. In summary, the formation of metallic superlattice provides with several routes for the enhancement of ANE such as

adding the interface-induced spin-orbit interaction and modulating the electronic structure. These strategies are useful to develop potential applications such as a heat flux sensor [Ref.34].

Section 2 also introduced the recent study demonstrating the suppression of thermal conduction in the perpendicular direction to the layer stacking [Ref. 62]. Although one of the merits of metallic superlattice has been demonstrated, the anisotropy of σ_{yy} to κ_{xx} was not so significant, resulting in the limited contribution to the improved zT. This means that the transverse thermoelectric coefficient still plays a major role for the thermoelectric conversion performance of metallic superlattice. Considering these facts, it is an effective way to incorporate a magnetic layer itself possessing anisotropic transport properties, *e.g.* 2-dimensional layered material, into the superlattice structure. At the same time, it is still a crucial task to explore materials showing larger transverse thermoelectric coefficient. We expect a significant improvement of zT by incorporating the magnetic layer, which can satisfy the above requirements, into the superlattice structure.

In addition to the purpose of enhancement of ANE and the suppression of thermal conduction, metallic superlattices are suitable research subjects for studying the spin-dependent thermal transport [Ref.83-85] such thermal conductivity switching [Ref.86] although this review paper does not involve that research topic. We believe that metallic superlattices will provide a platform to examine a variety of spin-caloritronic phenomena.

Acknowledgements

The works introduced in this review article were done in collaboration with K. Ito, T. Kikkawa, T. Kubota, Y.-C. Lau, K. Masuda, A. Miura, Y. Miura, T. Oyake, Z. Qiu, E. Saitoh, Y. Sakuraba, J. Shiomi. M. Shirai, M. Tsujikawa, J. Wang, and W. Zhou. The authors are sincerely grateful to them. Those works were partly supported by Grant-in-Aid for Scientific Research (S) (Grant Nos.

JP18H05246 and JP22H04965) from JSPS KAKENHI and ERATO "Magnetic Thermal Management Materials" (Grant No. JPMJER2201) from JST.

References

[1] M. N. Baibich, J. M. Broto, A. Fert, F. Nguyen Van Dau, F. Petroff, P. Etienne, G. Creuzet, A. Friederich, and J. Chazelas, Phys. Rev. Lett. **61**, 2472 (1988).

[2] G. Binasch, P. Grünberg, F. Saurenbach, and W. Zinn, Phys. Rev. B, **39**, 4828(R) (1989).

[3] S. Maekawa, E. Saitoh, S. O. Valenzuela and T. Kimura (Eds.), "Spin Current (2nd Edition)" (Oxford Univ. Press, Oxford, 2017).

[4] K. Takanashi, Jpn. J. Appl. Phys. **49**, 110001 (2010).

[5] D.C. Ralph, M.D. Stiles, J. Magn. Magn. Mater. **320**, 1190 (2008).

[6] Y. Kajiwara, K. Harii, S. Takahashi, J. Ohe, K. Uchida, M. Mizuguchi, H. Umezawa, H. Kawai, K. Ando, K. Takanashi, S. Maekawa, and E. Saitoh, Nature **464**, 262 (2010).

[7] G. E. W. Bauer, E. Saitoh, and B. J. van Wees, Nat. Mater. **11**, 391-399 (2012).

[8] S. R. Boona, R. C. Myers and J. P. Heremans, Energy Environ. Sci. **7**, 885 (2014).

[9] K. Uchida, Proc. Jpn. Acad. Ser. B **97**, 69 (2021).

[10] M. Hatami, G. E. W. Bauer, Q. Zhang and P. J. Kelly, Phys. Rev. Lett. **99**, 066603 (2007).

[11] K. Uchida, S. Takahashi, K. Harii, J. Ieda, W. Koshibae, K. Ando, S. Maekawa, and E. Saitoh, Nature **455**, 778-781 (2008).

[12] K. Uchida, J. Xiao, H. Adachi, J. Ohe, S. Takahashi, J. Ieda, T. Ota, Y. Kajiwara, H. Umezawa, H. Kawai, G. E. W. Bauer, S. Maekawa and E. Saitoh, Nat. Mater. **9**, 894 (2010).

[13] K. Uchida, H. Adachi, T. Ota, H. Nakayama, S. Maekawa and E. Saitoh, Appl. Phys. Lett. **97**, 172505 (2010).

[14] Y. Tserkovnyak, A. Brataas and G. E. W. Bauer, Phys. Rev. Lett. **88**, 117601 (2002).

[15] A. Hoffman: IEEE Trans. Magn., **49** (2013), 5172-5192.

[16] J. Sinova, S. O. Valenzuela, J. Wunderlich, C. H. Back and T. Jungwirth, Rev. Mod. Phys. **87**, 1213

(2015).

[17] H. Masuda, R. Modak, T. Seki, K. Uchida, Y.-C. Lau, Y. Sakuraba, R. Iguchi, and K. Takanashi, Commun. Mater. **1**, 75 (2020).

[18] H. Masuda, T. Seki, Y.-C. Lau, T. Kubota, and K. Takanashi, Phys. Rev. B **101**, 224413 (2020).

[19] Y.-C. Lau, T. Seki, and K. Takanashi, APL Mater. **9**, 081113 (2021).

[20] Y.-C. Lau, J. Ikeda, K. Fujiwara, A. Ozawa, J. Zheng T. Seki, K. Nomura, L. Du, Q. Wu, A. Tsukazaki, and K. Takanashi, Phys. Rev. B **108**, 064429 (2023).

[21] T. Seki, Y.-C. Lau, J. Ikeda, K. Fujiwara, A. Ozawa, S. Iihama, K. Nomura, and A. Tsukazaki, Phys. Rev. Research **5**, 013222 (2023).

[22] A. Slachter, F. L. Bakker, J. Adam, and B. J. Van Wees, Nat. Phys. **6**, 879 (2010).

[23] J. Flipse, F. L. Bakker, A. Slachter, F. K. Dejene and B. J. van Wees, Nat. Nanotehch. **7**, 166 (2012).

[24] J. Flipse, F. K. Dejene, D. Wagenaar, G. E. W. Bauer, J. Ben Youssef and B. J. van Wees, Phys. Rev. Lett. **113**, 027601 (2014).

[25] S. Daimon, R. Iguchi, T. Hioki, E. Saitoh and K. Uchida, Nat. Commun. **7**, 13754 (2016).

[26] S. Meyer, Y.-T. Chen, S. Wimmer, M. Althammer, T. Wimmer, R. Schlitz, S. Geprägs, H. Huebl, D. Ködderitzsch, H. Ebert, G. E. W. Bauer, R. Gross & S. T. B. Goennenwein, Nat. Mater. **16**, 977 (2017).

[27] P. Sheng, Y. Sakuraba, Y.-C. Lau, S. Takahashi, S. Mitani, and M. Hayashi, Sci. Adv. **3**, e1701503 (2017).

[28] K. Uchida, W. Zhou, and Y. Sakuraba, Appl. Phys. Lett. **118**, 140504 (2021).

[29] Y. Sakuraba, K. Hyodo, A. Sakuma, and S. Mitani, Phys. Rev. B **101**, 134407 (2020).

[30] T. Seki, R. Iguchi, K. Takanashi and K. Uchida, Appl. Phys. Lett. **112**, 152403 (2018).

[31] T. Seki, R. Iguchi, K. Takanashi, and K. Uchida, J. Phys. D: Appl. Phys. 51, 254001 (2018).

[32] K. Uchida and J. P. Heremans, Joule **6**, 2240 (2022).

[33] Y. Sakuraba, Scri. Mater. **111**, 29 (2016).

[34] W. Zhou and Y. Sakuraba, Appl. Phys. Express, **13**, 043001 (2020).

[35] K. Uchida, Nat. Mater. **21**, 136 (2022).

[36] A. Sakai, Y. P. Mizuta, A. A. Nugroho, R. Sihombing, T. Koretsune, M.-T. Suzuki, N. Takemori, R. Ishii, D. Nishio-Hamane, R. Arita, P. Goswami, and S. Nakatsuji, Nat. Phys. **14**, 1119 (2018).

[37] K. Sumida, Y. Sakuraba, K. Masuda, T. Kono, M. Kakoki, K. Goto, W. Zhou, K. Miyamoto, Y. Miura, T. Okuda, and A. Kimura, Commun. Mater. **1**, 89 (2020).

[38] A. Miura, H. Sepehri-Amin, K. Masuda, H. Tsuchiura, Y. Miura, R. Iguchi, Y. Sakuraba, J. Shiomi, K. Hono, and K. Uchida, Appl. Phys. Lett. **115**, 222403 (2019).

[39] R. Modak, Y. Sakuraba, T. Hirai, T. Yagi, H. Sepehri-Amin, W. Zhou, H. Masuda, T. Seki, K. Takanashi, T. Ohkubo and K. Uchida, Sci. Tech. Adv. Mater. **23**, 767-782 (2022).

[40] H. Nakayama, K. Masuda, J. Wang, A. Miura, K. Uchida, M. Murata, and Y. Sakuraba, Phys. Rev. Mater. **3**, 114412 (2019).

[41] A. Sakai, S. Minami, T. Koretsune, T. Chen, T. Higo, Y. Wang, T. Nomoto, M. Hirayama, S. Miwa, D. Nishio-Hamane, F. Ishii, R. Arita, and S. Nakatsuji, Nature **581**, 53 (2020).

[42] H. Reichlova, R. Schlitz, S. Beckert, P. Swekis, A. Markou, Y. Chen, D. Kriegner, S. Fabretti, G. H. Park, A. Niemann, S. Sudheendra, A. Thomas, K. Nielsch, C. Felser, and S. T. B. Goennenwein, Appl. Phys. Lett. **113**, 212405 (2018).

[43] S. N. Guin, P. Vir, Y. Zhang, N. Kumar, S. J. Watzman, C. Fu, E. Liu, K. Manna, W. Schnelle, J. Gooth, C. Shekhar, Y. Sun, and C. Felser, Adv. Mater. **31**, 1806622 (2019).

[44] S. Noguchi, K. Fujiwara, Y. Yanagi, M.-T. Suzuki, T. Hirai, T. Seki, K. Uchida, and A. Tsukazaki, Nat. Phys. **20,** 254-260 (2024).

[45] T. Asaba, V. Ivanov, S. M. Thomas, S. Y. Savrasov, J. D. Thompson, E. D. Bauer, and F. Ronning, Sci. Adv. **7**, eabf1467 (2021).

[46] P. F. Carcia, A. D. Meinhaldt, and A. Suna, Appl. Phys. Lett. **47**, 178 (1985).

[47] P. Grünberg, R. Schreiber, Y. Pang, M. B. Brodsky, and H. Sowers, Phys. Rev. Lett. **57**, 2442 (1986).

[48] J. A. C. Bland and B. Heinrich (Eds.), "Ultrathin magnetic structures I" (Springer, Verlag Berlin Heidelberg, 2005).

[49] T. Yamazaki, T. Seki, R. Modak, K. Nakagawara, T. Hirai, K. Ito, K. Uchida, and K. Takanashi, Phys. Rev. B **105**, 214416 (2022).

[50] K. Uchida, T. Kikkawa, T. Seki, T. Oyake, J. Shiomi, Z. Qiu, K. Takanashi and E. Saitoh, Phys. Rev. B **92**, 094414 (2015).

[51] S. Y. Huang, X. Fan, D. Qu, Y. P. Chen, W. G. Wang, J. Wu, T. Y. Chen, J. Q. Xiao, and C. L. Chien, Phys. Rev. Lett. **109**, 107204 (2012).

[52] Y. M. Lu, Y. Choi, C. M. Ortega, X. M. Cheng, J. W. Cai, S. Y. Huang, L. Sun, and C. L. Chien, Phys. Rev. Lett. **110**, 147207 (2013).

[53] H. Ibach and H. Lüth, Solid-State Physics: An Introduction to Principles of Materials Science (Springer, Berlin, 2009).

[54] D. A. Papaconstantopoulos, Handbook of the Band Structure of Elemental Solids (Plenum, New York, 1986).

[55] S. Geprägs, S. Meyer, S. Altmannshofer, M. Opel, F. Wilhelm, A. Rogalev, R. Gross, and S. T. B. Goennenwein, Appl. Phys. Lett. **101**, 262407 (2012).

[56] T. Kikkawa, K. Uchida, Y. Shiomi, Z. Qiu, D. Hou, D. Tian, H. Nakayama, X.-F. Jin, and E. Saitoh, Phys. Rev. Lett. **110**, 067207 (2013).

[57] C. Fang, C. H. Wan, Z. H. Yuan, L. Huang, X. Zhang, H. Wu, Q. T. Zhang, and X. F. Han, Phys.

Rev. B **93**, 054420 (2016).

[58] R. Ramos, T. Kikkawa, M. H. Aguirre, I. Lucas, A. Anadón, T. Oyake, K. Uchida, H. Adachi, J. Shiomi, P. A. Algarabel, L. Morellón, S. Maekawa, E. Saitoh, and M. R. Ibarra, Phys. Rev. B **92**, 220407(R) (2015).

[59] R. Ramos, A. Anadón, I. Lucas, K. Uchida, P. A. Algarabel, L. Morellón, M. H. Aguirre, E. Saitoh, and M. R. Ibarra, APL Mater. **4**, 104802 (2016).

[60] K. Uchida, R. Iguchi, S. Daimon, R. Ramos, A. Anadón, I. Lucas, P. A. Algarabel, L. Morellón, M. H. Aguirre, M. R. Ibarra, and E. Saitoh, Phys. Rev. B **95**, 184437 (2017).

[61] R. Ramos, T. Kikkawa, A. Anadón, I. Lucas, T. Niizeki, K. Uchida, P. A. Algarabel, L. Morellón, M. H. Aguirre, M. R. Ibarra, and E. Saitoh, Appl. Phys. Lett. **114**, 113902 (2019).

[62] T. Yamazaki, T. Hirai, T. Yagi, Y. Yamashita, K. Uchida, T. Seki, and K. Takanashi, Phys. Rev. Applied **21**, 024039 (2024).

[63] K. Uchida, S. Daimon, R. Iguchi, and E. Saitoh, Nature **558**, 95 (2018).

[64] K. Masuda, K. Uchida, R. Iguchi, and Y. Miura, Phys. Rev. B **99**, 104406 (2019).

[65] T. Seki, Y. Sakuraba, K. Masuda, A. Miura, M. Tsujikawa, K. Uchida, T. Kubota, Y. Miura, M. Shirai, and K. Takanashi, Phys. Rev. B **103**, L020402 (2021).

[66] T. Seki, M. Tsujikawa, K. Ito, K. Uchida, H. Kurebayashi, M. Shirai, and K. Takanashi, Phys. Rev. Mater. **4**, 064413 (2020).

[67] A. Miura, R. Iguchi, T. Seki, K. Takanashi, and K. Uchida, Phys. Rev. Mater. **4**, 034409 (2020).

[68] N. F. Mott and H. Jones, in The Theory of the Properties of Metals and Alloys (Clarendon, Oxford, 1936), pp. 308–314.

[69] G.-H. Park, H. Reichlova, R. Schlitz, M. Lammel, A. Markou, P. Swekis, P. Ritzinger, D. Kriegner, J. Noky, J. Gayles, Y. Sun, C. Felser, K. Nielsch, S. T. B. Goennenwein, and A. Thomas, Phys. Rev.

B **101**, 060406(R) (2020).

[70] H. Isshiki, Z. Zhu, H. Mizuno, R. Uesugi, T. Higo, S. Nakatsuji, and Y. Otani, Phys. Rev. Mater. **6**, 084411 (2022).

[71] Q. Wang, Z. Wen, T. Kubota, T. Seki, and K. Takanashi, Appl. Phys. Lett. **115**, 252401 (2019).

[72] K. Tang, Z. Wen, Y.-C. Lau, H. Sukegawa, T. Seki, and S. Mitani, Appl. Phys. Lett. **118**, 062402 (2021).

[73] S. Trolier-McKinstry and P. Muralt, J. Electroceram. **12**, 7 (2004).

[74] K. Tonisch, V. Cimalla, C. Foerster, D. Dontsov and O. Ambacher, Phys. Status Solidi C **3**, 2274 (2006).

[75] P. Muralt, J. Am. Ceram. Soc. **91**, 1385 (2008).

[76] Y. X. Yu, J. Shi, and Y. Nakamura, Acta Mater. **60**, 6770 (2012).

[77] Y. X. Yu, L. Wang, J. Shi, and Y. Nakamura, J. Phys. Chem. Solids **75**, 1301 (2014).

[78] J. Wang, Y.-C. Lau, W. Zhou, T. Seki, Y. Sakuraba, T. Kubota, K. Ito, and K. Takanashi, Adv. Electron. Mater. **8**, 2101380 (2022).

[79] A. Miyashita, M. Maekawa, C. Suzuki, S. Yamamoto, A. Kawasuso, J. Wang, T. Seki, R. Y. Umetsu, and K. Takanashi, J. Appl. Phys. **130**, 225301-1-7 (2021).

[80] M. Irfan, Z. Abbas, S. Khan, M. Sohail, M. Rani, S. Azam and I. V. Kityk, J. Alloys Compd. **750**, 804 (2018).

[81] D. Kan and Y. Shimakawa, Appl. Phys. Lett. **115**, 022403 (2019).

[82] S. Ahmad, F. Khan, B. Amin, and I. Ahmad, J. Solid State Chem. **299**, 122189 (2021).

[83] H. Sato, Y. Aoki, Y. Kobayashi, H. Yamamoto, and T. Shinjo, J. Phys. Soc. Jpn. **62**, 431 (1993).

[84] H. Sato, H. Henmi, Y. Kobayashi, Y. Aoki, H. Yamamoto, T. Shinjo, and V. Sechovsky, J. Appl. Phys. **76**, 6919 (1994).

[85] J. Kimling, R. B. Wilson, K. Rott, J. Kimling, G. Reiss, and D. G. Cahill, Phys. Rev. B **91**, 144405 (2015).

[86] H. Nakayama, B. Xu, S. Iwamoto, K. Yamamoto, R. Iguchi, A. Miura, T. Hirai, Y. Miura, Y. Sakuraba, J. Shiomi, and K. Uchida, Appl. Phys. Lett. **118**, 042409 (2021).

Table 1 Representative ferromagnetic materials showing anomalous Nernst coefficient (S_{ANE}) larger than 1 μV K^{-1} at room temperature.

Material	Form	S_{ANE} (μV K^{-1})	Ref.
Co_2MnGa	Slab	6	36
Co_2MnGa	Thin film	6.2	37
$SmCo_5$	Slab	3.1	38
Sm-Co-Fe	Thin film	1.6	39
Fe-Ga	Thin film	2.4	40
Fe_3Ga	Slab	6	41
Fe-Al	Thin film	3.4	34
Fe_3Al	Slab	4	41

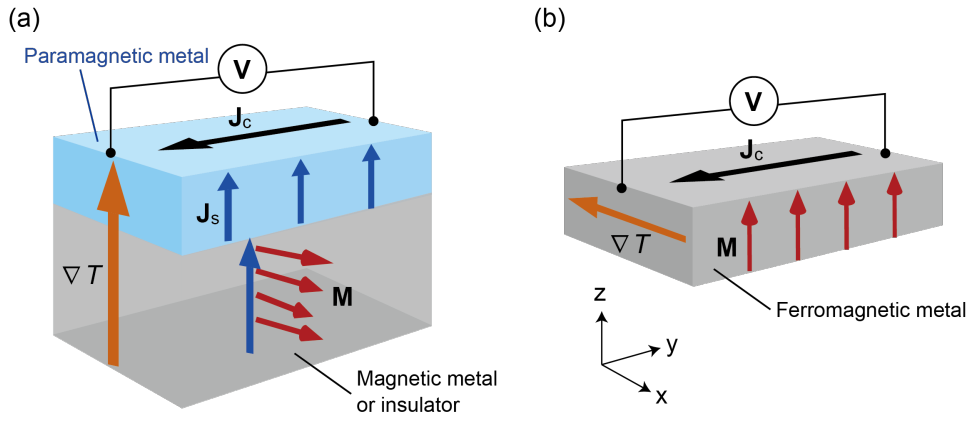

Figure 1 (a) Spin Seebeck effect observed in a junction with a magnetic material and a conductor. Spin current ($\mathbf{j}_s$) is induced near the junction interface by applying the temperature gradient (∇T) in the junction. This $\mathbf{j}_s$ is converted into $\mathbf{j}_c$ via inverse spin Hall effect. (b) Anomalous Nernst effect observed in a ferromagnetic thin film with spontaneous magnetization ($\mathbf{M}$). When the temperature gradient of ∇T is applied along the *x* direction, the charge current flow appears along the *y* direction.

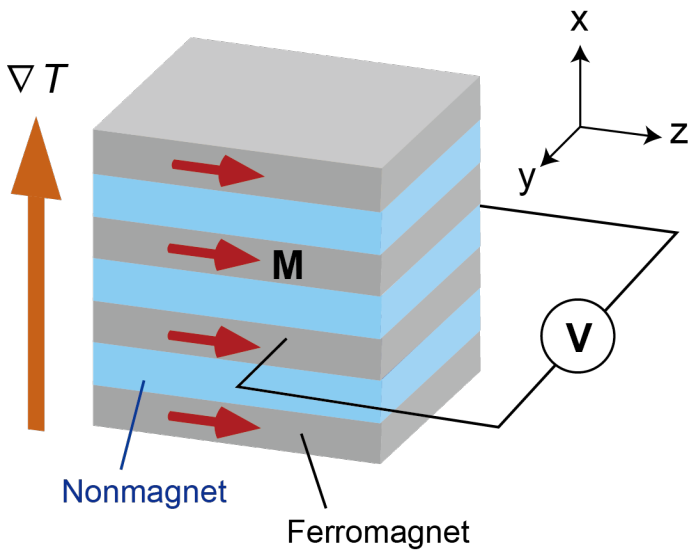

Figure 2 Illustration for the configuration of the ANE utilizing the metallic superlattice, in which ferromagnetic layers with **M** and nonmagnetic layers are alternatively stacked.

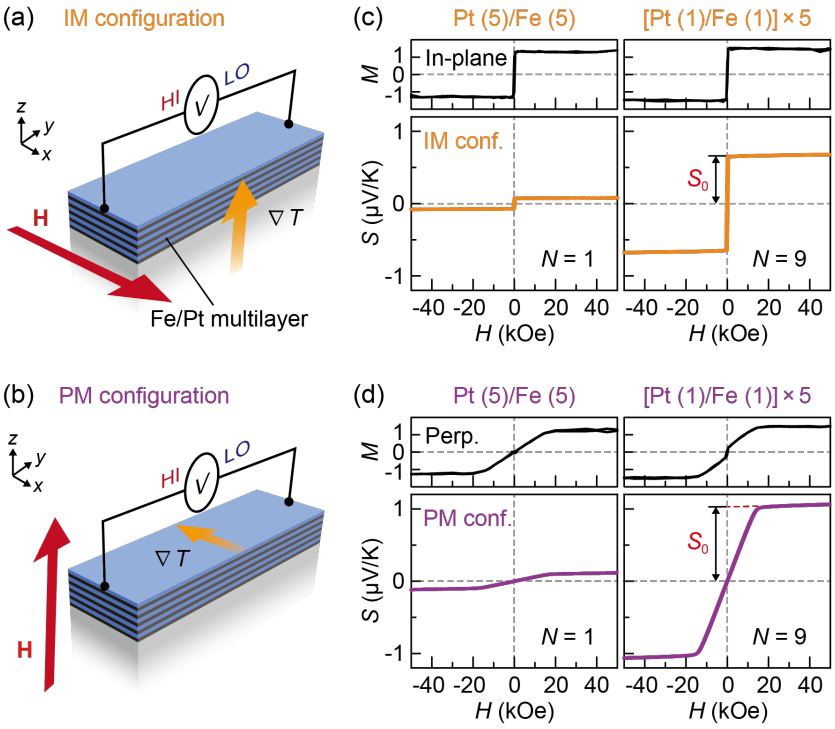

Figure 3 (a), (b) Schematic illustrations of the Fe/Pt multilayer sample in the (a) in-plane magnetized (IM) and (b) perpendicularly magnetized (PM) configurations. **H** denotes the magnetic field vector with the magnitude of H. (c) The in-plane magnetization curve and the H dependence of the transverse thermopower S for the (5)/Fe (5) and [Pt (1)/Fe (1)]$_{\times 5}$ samples. M denotes the total magnetization (in units of kemu/cm^3) of the Fe/Pt multilayer samples formed on thermally oxidized silicon substrates. In the M-H curves, the contributions from the silicon substrates are subtracted. S_0 is the anomalous component of S, obtained by extrapolating the S-H curve in the high H field range to zero field. (d) The perpendicular magnetization curve and the H dependence of S for the (5)/Fe (5) and [Pt (1)/Fe (1)]$_{\times 5}$ samples. [Ref.50]

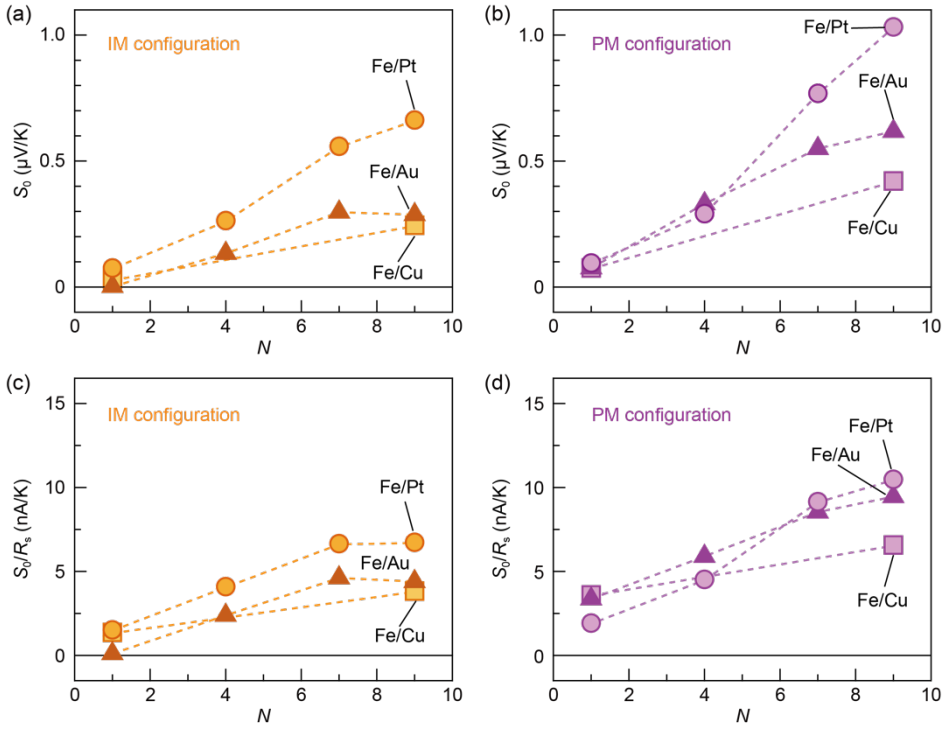

Figure 4 (a) N dependence of S_0 in the Fe/Pt, Fe/Au, and Fe/Cu samples in the IM and (b) PM configurations. The Fe/Cu multilayer samples are covered with 1-nm-thick Pt films to avoid the oxidation of the top Cu layers. (c) N dependence of S_0/R_s in the Fe/Pt, Fe/Au, and Fe/Cu samples in the IM and (d) PM configurations, where R_S is the sheet resistance. [Ref.50]

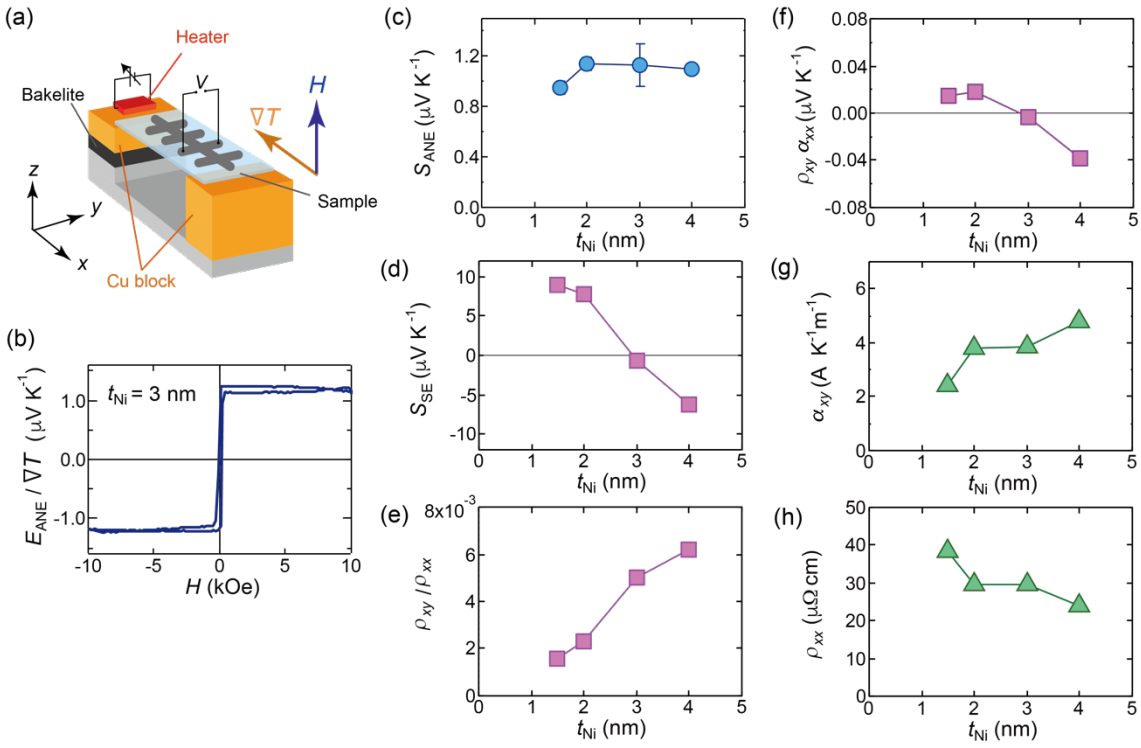

Figure 5 (a) Illustration of experimental setup for measuring the ANE in the PM configuration for [Ni(t_{Ni})/Pt(1.0 nm)]$_{\times n}$ metallic superlattices. (b) H dependence of electric field induced by the ANE (E_{ANE}) divided by ∇T for the device with t_{Ni} = 3.0 nm. (c) Anomalous Nernst coefficient (S_{ANE}), (d) Seebeck coefficient (S_{SE}), (e) the ratio of anomalous Hall resistivity to longitudinal resistivity (ρ_{xy}/ρ_{xx}), (f) the product of ρ_{xy} and longitudinal thermoelectric conductivity (α_{xx}), (g) transverse thermoelectric conductivity (α_{xy}), and (h) ρ_{xx} as a function of t_{Ni} [Ref. 65].

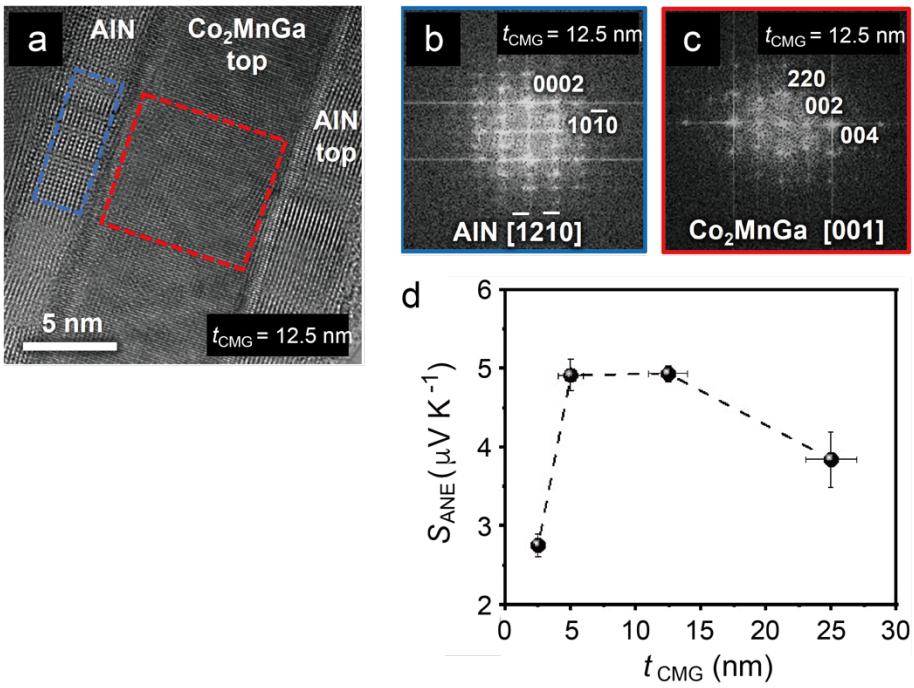

Figure 6 (a) Cross-sectional high-resolution transmission electron microscopy image for the AlN (20.0 nm)/ [Co_2MnGa (CMG) (t_{CMG} = 12.5 nm)/AlN (5.0 nm)]$_{\times 2}$, and (b) the fast Fourier transform images for the CMG and (c) AlN layers. (d) S_{ANE} as a function of t_{CMG} [Ref.78].